Chinese Journal of Chemical Engineering 53 (2023) 124–132

Contents lists available at ScienceDirect

Chinese Journal of Chemical Engineering

journal homepage: www.elsevier.com/locate/CJChE

Full Length Article

Insight into the dynamic adsorption behavior of graphene oxide multichannel architecture toward contaminants

Jian Tian [1], Gen Li [1], Wang He [1], Kok Bing Tan [1], Daohua Sun [1,*], Junfu Wei [2,*], Qingbiao Li [1,3]

[1] Department of Chemical and Biochemical Engineering, College of Chemistry and Chemical Engineering, Xiamen University, Xiamen 361005, China
[2] College of Chemistry and Chemical Engineering, Tiangong University, Tianjin 300387, China
[3] College of Food and Biological Engineering, Jimei University, Xiamen 361021, China

ARTICLE INFO

Article history:
Received 7 July 2021
Received in revised form 3 December 2021
Accepted 16 December 2021
Available online 26 February 2022

Keywords:
Graphene oxide
Multichannel
Adsorptive behavior
Phenol
DFT calculations

ABSTRACT

Graphene oxide (GO) channels exhibit unique mass transport behaviors due to their flexibility, controllable thinness and extraordinary physicochemical properties, enabling them to be widely used for adsorption and membrane separation. Nevertheless, the adsorption behavior of nanosized contaminants within the channels of GO membrane has not been fully discussed. In this study, we fabricated a GO membrane (PG*n*, where *n* represents the deposition cycles of GO) with multi channels *via* the cross-linking of GO and multibranched poly(ethyleneimine) (PEI). Phenol was used as molecular probe to determine the correlations between dynamic adsorption behavior and structural parameters of the multilevel GO/PEI membrane. PG8 shows higher adsorption capacities and affinity, which is predominantly attributed to the multichannel structure providing a large specific surface for phenol adsorption, enhancing the accessibility of active sites for phenol molecules and the transport of phenol. Density functional theory calculations demonstrate that the adsorption mechanism of phenol within GO channel is energetically oriented by hydrogen bonds, which is dominated by oxygen-containing groups compared to amino groups. Particularly, the interfaces which facilitate strong π-π interaction and hydrogen bonds maybe the most active regions. Moreover, the as-prepared PG8 membrane showed outstanding performance for other contaminants such as methyl orange and Cr(VI). It is anticipated that this study will have implications for design of GO-related environmental materials with enhanced efficiency.

1. Introduction

Mechanical properties and excellent adsorption capacity of graphene oxide (GO) contributed to extensive applications in water purification [1–5]. Particularly, an intriguing surface chemistry is imparted by the unique structural characteristics of GO, making it highly amenable to various contaminants [6]. The highly delocalized π-electron system of GO is crucial because it enables strong π-π stacking interactions with organic compounds [7]. Therefore, GO has outstanding adsorptive capabilities toward organic contaminants. In addition, GO possesses abundant oxygen-containing groups on its basal plane and edges, including hydroxyl, carboxyl and epoxy groups [8]. As a result, GO can capture heavy metal ions *via* electrostatic interaction and chelation mechanism [9–12]. Nevertheless, using GO as an adsorbent for dynamic adsorption may be difficult, as the tiny size of GO makes them difficult to recover or recycle and prone to secondary contamination [13,14]. Moreover, the build-up of GO is often unavoidable due to van der Waals forces, leading to a reduction of binding sites with contamination.

Several approaches have been proposed to eliminate these problems, including fabricating GO membranes, building GO-based 3D macrostructures, or binding GO to supports. Among them, GO membranes have received extensive attention due to their fast permeation kinetics and extraordinary separation capability [15]. The space between two neighboring GO forms a nanosized channel that allows water to pass through [16,17]. Meanwhile, the oxygen functional groups on the GO surface could provide convenient sites for further functionalization to enhance properties such as interactions and charges with water contaminants [18,19]. In this regard, the stacking of GO sheets provides the well-defined carbon channels for water purification that allow the flow of a water fluid while rejecting unwanted species [20–22]. Thus, the GO membranes are considered to be suitable for water purification.

* Corresponding authors.
E-mail addresses: sdaohua@xmu.edu.cn (D. Sun), jfwei@tjpu.edu.cn (J. Wei).

https://doi.org/10.1016/j.cjche.2021.12.029
1004-9541/

Researchers have conducted extensive studies on GO membranes with excellent adsorption ability. Rodrigues *et al.* optimized the amounts of poly(enthyleneimine) (PEI), GO, chitosan, and glutaraldehyde to produce a multilayer GO membrane with outstanding adsorption ability of heavy metals [23]. Liu *et al.* intercalated nanocrystals into interlayered GO membrane, greatly enhancing the adsorption performance of methylene blue and Congo red [24]. In addition, Sitko *et al.* [25] prepared a durable multilayer GO membrane by noncovalent interaction using oxidized CNTs. The excellent stability of the GO membrane enables the effective adsorption of metal ions under different pH values, flow conditions and severe vibration conditions. Many studies have been conducted on the adsorption properties or stability of GO membranes, but the adsorption behavior involved in GO channels has not been fully explored so far. In this study, we shed light on the diffusion behavior and adsorption mechanisms through GO membranes, which depend on the multichannel structure and active sites of GO.

Phenol is an economically efficient chemical product which is widely used in dyes, fungicides, preservatives, pharmaceuticals and other applications [26–28]. However, phenol is also a highly toxic and hard-to-degrade substance which can cause cellular inactivation through denaturation of proteins in living organisms. Herein, PEI and GO were employed as building blocks for the construction of multichannel architecture of membrane and was used in a dynamic adsorption toward phenol. The correlations between adsorption behavior and structural parameters of the multilevel GO membrane was systematically investigated by Fick's second law and intraparticle diffusion model. In addition, the favorable adsorption sites of GO channel were further explored by DFT calculations.

2. Experimental

2.1. Materials

Graphene oxide (GO) was obtained from Tianjin Kermel Chemical Regent Ltd. Phenol, acrylamide (AM), benzophenone (BP), sodium diethyldithiocarbamate (SDC), poly(ethyleneimine) (PEI), methyl orange (MO) and Cr (VI) were purchased from Aladdin (Shanghai, China) and Tengzhun Biotechnology Co. Ltd. (Shanghai, China), respectively. Polypropylene (PP) nonwoven (50 $g{\cdot}m^2$) was purchased from Haidexin Chemical Factory (Jiangsu, China).

2.2. Fabrication of PG*n*

The preparation route of PG*n* membrane is shown in Fig. 1. The fabrication of polypropylene support grafted by acrylamide (PP-*g*-AM) is shown in Supplementary Material. Layer-by-layer (LbL) approach was employed to deposit GO onto PP-*g*-AM followed by cross-linking with PEI to enhance structural stability. The as-prepared PP-*g*-AM was put into GO suspension (0.1 $mg{\cdot}ml^{-1}$), and oscillated for 20 min. Upon washing with deionized water, the sample was dipped into a PEI solution (0.1 $mg{\cdot}ml^{-1}$) and was followed by a new deposition cycle. The PG*n* membrane was dried at 90 °C to facilitate the cross-linking between GO and PEI, followed by soaked in ethanol to remove the unbonded GO. The obtained sample was labeled as PG*n*, where *n* represents the number of deposition cycles of graphene oxide on the substrate.

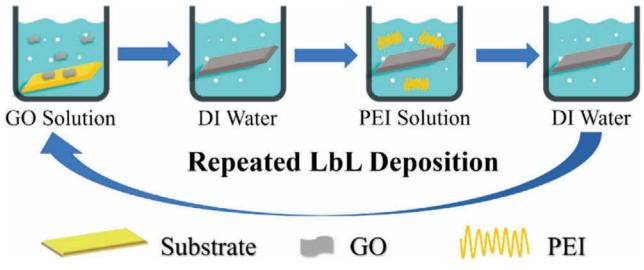

Fig. 1. Schematic process for the fabrication of PG*n* membrane (*n* representing the number of deposition cycles) *via* LbL deposition of GO and PEI.

2.3. Characterization

The morphology of the sample's surface was conducted on Hitachi S-4800 scanning electron microscopy (SEM) microscope. Necolet 6700 (Thermo Fisher, USA) analyzed the surface composition by Fourier transform infrared (FT-IR) spectrometer over the wavelength range of 4000–500 cm^{-1}. X-ray photoelectron spectroscopy (XPS) with AEM PHI 5300X spectrometer was used to verify the functional group. The GO deposition cycles were characterized by UV absorption spectra with a Lambda 35-vis (Perkin Elmer, America) spectrometer range of 200–400 nm. The surface area and pore size distribution of PG*n* were analyzed on a Gemini VII instrument (Micromeritics, America) by Brunauer-Emmett-Teller (BET) method. The wettability of samples was tested by KRUSS DSA100 contact angle analyzer. The sample's surface potential was conducted using a Nano-ZS90 Zetasizer (Malvern Instruments Ltd., UK) to verify electrostatic interaction of PG*n* and contaminants.

2.4. Adsorption experiment

Under the initial concentration of phenol at 50 $mg{\cdot}L^{-1}$, dynamic adsorption of phenol was performed by a continuous-flow filtration experiment. The pH was adjusted by NaOH and HCI solution to maintain about 6.5. Phenol solution was passed through the filter and the pollutant stock solution was then pushed through the multilayer PG*n* with a peristaltic pump. The concentration of filtrate was measured with a UV–vis spectrophotometer. The following equation determined the accumulative adsorption capability of PG*n*:

$$q_{ad} = \int_0^t \frac{Q(C_0 - C_t)}{1000M} dt \quad (1)$$

where q_{ad} ($mg{\cdot}g^{-1}$), Q ($ml{\cdot}min^{-1}$), M (g), C_0 ($mg{\cdot}L^{-1}$) and C_t ($mg{\cdot}L^{-1}$) are the accumulative adsorption amount, flow rate, adsorbent mass, initial and residual concentration of pollutant, respectively.

The adsorption experiments were carried out with batch techniques with an initial concentration of 50 $mg{\cdot}L^{-1}$ for phenol. Phenol was dissolved in water and then 50 mg of adsorbent was added in the flask, which is placed in an incubator at 25 °C. The phenol concentrations were performed at different time by UV–Vis spectrometer. The equilibrium adsorption capability of PG*n* was determined by the following:

$$q_e = \frac{(C_0 - C_e) \times V}{M} \quad (2)$$

where q_e, V (ml), C_0 and C_e are the amount adsorbed, volume of the solution, initial and equilibrium concentration, respectively.

2.5. DFT calculations

According to the projection augmented wave (PAW) method, the Vienna Ab initio Simulation Package (VASP) code was performed for the DFT calculations. The geometry optimization calculations of the proposed models were performed using the generalized gradient approximation (GGA) with the Perdew-Burkee-Ernzerhof (PBE) functional. The k-point meshes were set as 3 × 3 × 1 that automatically generated by using the Monkhorst-Pack method and the cut-off energy was set as 450 eV. To eliminate interactions of the periodic structures, the

vacuum layer was built to be 1.5 nm. The convergence thresholds for geometry optimization calculations of all the models were set as 1.0×10^{-5} eV per atom, 1.0×10^{-4} nm for displacement, and 3.0×10^{-3} eV·nm^{-1} for force. The self-consistent convergence tolerance was set at 1.0×10^{-5} eV per atom.

3. Results and Discussion

3.1. Characterization of multichannel PGn

Fig. 2(a)–(d) display typical digital photos of PP-*g*-AM, PG2, PG4 and PG8. As shown in Fig. 2(e) and Fig. S1 (in Supplementary Material), PP-*g*-AM substrate shows a porous surface, which exhibits a penetrate pore with an average size of 12 μm. The overlapped and intertwined structure of the substrate with large size porosity ensures smooth water penetration [29,30]. Furthermore, the corresponding characterizations of GO, such as SEM image, UV absorption spectrum, FTIR spectrum, and BET results are shown in Fig. S2 and S3. With the LbL deposition of GO sheets, the color of support with a diameter of 7.5 cm entirely turned black from white. As displayed in Fig. 2(g) and (h), in contrast with PG2 (Fig. 2(f)), a continuous GO layer completely covered the surfaces of PG4 and PG8 and no defect was observed. The deposited GO sheet manifests an evident heterogeneous exterior and stacking structure. Due to the face-to-face repulsive electrostatic forces of GO, disordered and loose channels were generally formed.

Cross section observation is illustrated as Fig. 3(a). The quasi-ordered laminar structure is consisted of the stacked interlamination between neighboring GO sheets. The amine groups on PEI are considered to integrate with carboxyl groups on GO. However, the disordered GO layers cannot be estimated by the SEM. Thus, the construction of films was further characterized by UV–vis absorption spectra. Fig. 3(b) validates the connection of absorbance at 220 nm *versus* the deposition unit number. The absorbance was found to increase with the deposition cycles, indicating a growth in thickness of GO [31]. In addition, the deposited amount of GO per cycle was found to be inconstant, suggesting relatively irregular growth of the film. Meanwhile, with the increasing content of GO and PEI, the water contact angles gradually decreased from 58.7° to 44.9° (Fig. S4). As displayed in Fig. 3(c), a broad peak from 3000 cm^{-1} to 3600 cm^{-1} emerged in the FT-IR spectrum corresponding to stretching vibration of —OH. With increasing deposition cycles, the hydrogen-bonded peak assigned to —OH was moved from 3350 cm^{-1} to 3245 cm^{-1}, confirming the formation of hydrogen bond in GO and PEI [32]. The peak at 1726 cm^{-1} is generated by C=O stretching vibrations on the carboxyl group, which disappear with increasing PEI deposition cycles. Meanwhile, peaks at 1638 cm^{-1} and 1466 cm^{-1} attributed to the N—H and C—N stretching on amide bonds were progressively enhanced [33]. The density of C—N covalent bond peaks increases with the number of deposited units, which is further confirmed by XPS. (Fig. S5) [34].

As shown in Fig. 4(a), the N_2 adsorption–desorption isotherms for PG2 can be acknowledged as Type II, indicating the typical physical adsorption process on adsorbents without pores or possessing macroporous. It was observed that the N_2 adsorption amount related to PG8 was significantly prolonged at low pressure (P/P_0 < 0.1), indicating the existence of micropores in PG8 [35]. Besides, H4 type hysteresis loop was noted, attributed the slit-shaped mesoporous formed by stacking GO [36]. The surface area of PG2, PG4 and PG8 were determined to be 11.86 m^2·g^{-1}, 45.87 m^2·g^{-1} and 68.11 m^2·g^{-1}, respectively. During the adsorption process, PG8 can provide a rich solid–liquid interface and promote the accumulation of organic molecules. As can be seen from Fig. 4(b), the pore size distribution of PG8 were determined to be mainly range from 2 to 30 nm. The multiscale porous structure is conducive to an accessible surface, thus enhance the molecule transfer and adsorption performance [37].

3.2. Dynamic adsorption toward phenol

The phenol breakthrough curves of hybrid PG*n* membranes were recorded and demonstrated in Fig. 5(a). As the GO deposition cycle increases, there is more potential for phenol to reach the active site of the GO film, thus reducing the outlet concentration. The individual dynamic adsorption capacities of PG2, PG4 and PG8 for phenol were determined to be 6.68 mg·g^{-1}, 13.32 mg·g^{-1} and 21.14 mg·g^{-1}, respectively. According to BET, the PG8 exhibited a large surface area and multiscale porous structure. Moreover, the combination of FT-IR and XPS study also showed that PG8 possessed more surface-active sites. Therefore, this may be due to its multi-channel structure, which provides an abundant solid–liquid interface for the adsorption of phenol, enabling transport of phenol and ensuring the accessibility of the active site of phenol.

From the fundamental point of view, the adsorption properties of PG*n* were affected by the multichannel architecture. Fick's second law was attained to investigate the diffusion properties of PG2, PG4 and PG8 [38,39]:

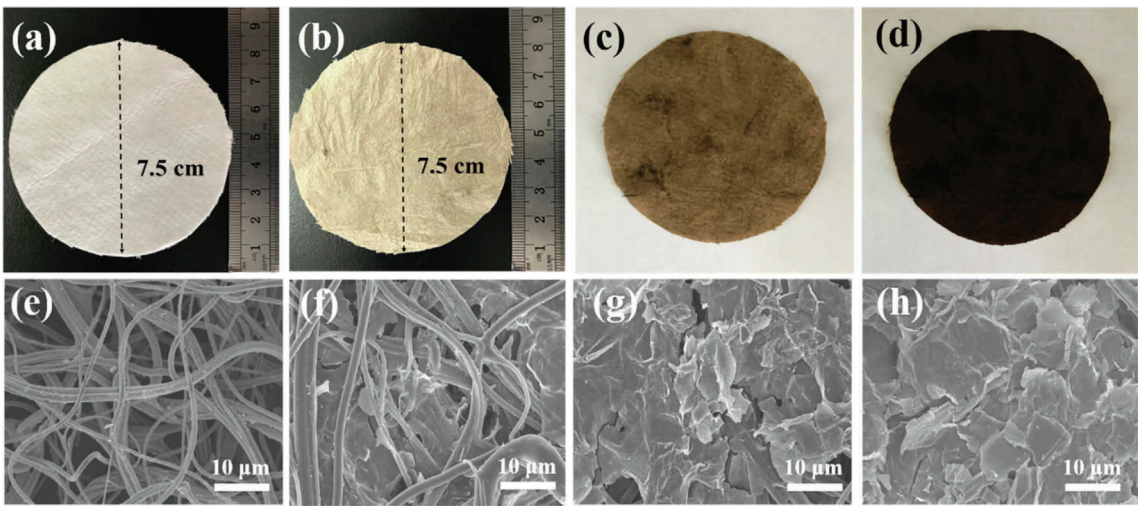

Fig. 2. Images of (a) PP-*g*-AM, (b) PG2, (c) PG4 and (d) PG8; SEM images of (e) PP-*g*-AM, (f) PG2, (g) PG4 and (h) PG8.

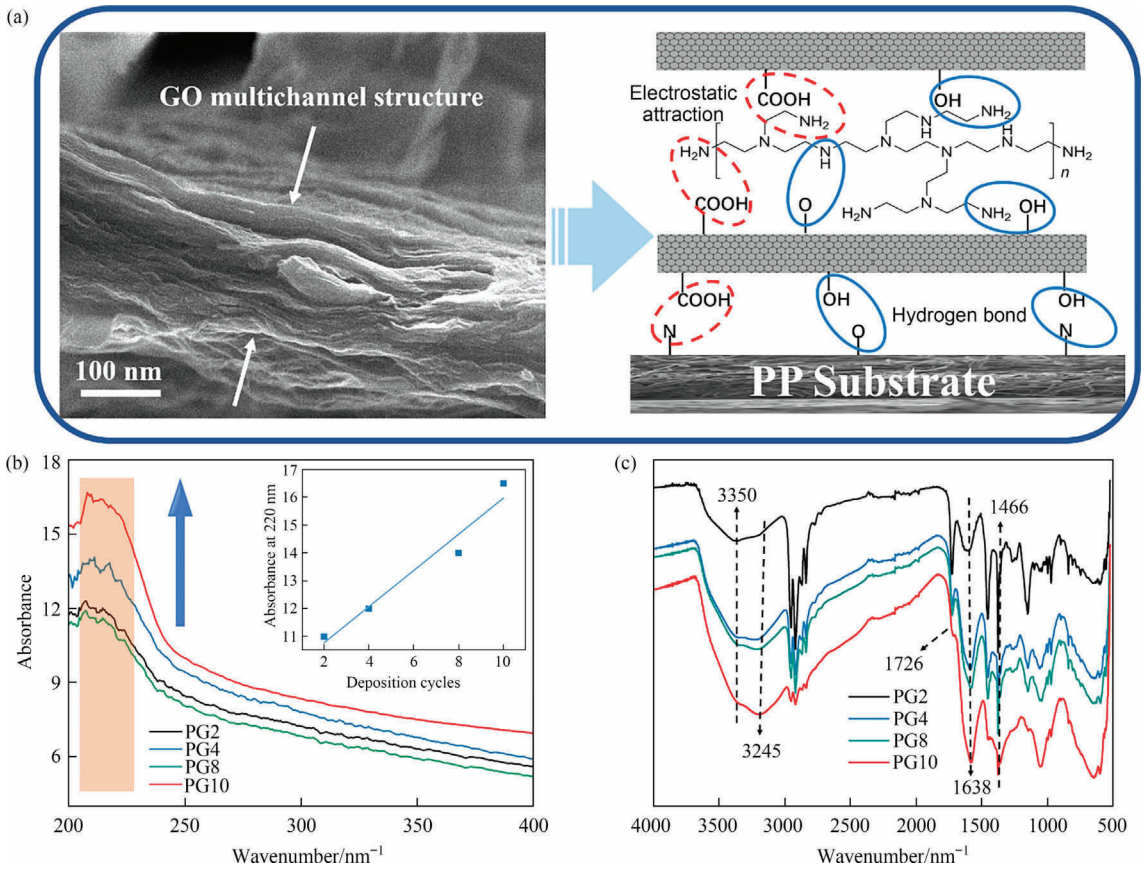

Fig. 3. (a) SEM cross sections of PG8; (b) UV absorption spectra of PG2, PG4 PG8 and PG10 and absorbance at 220 nm *versus* the number of deposition cycles; (c) FTIR spectra of PG2, PG4 PG8 and PG10.

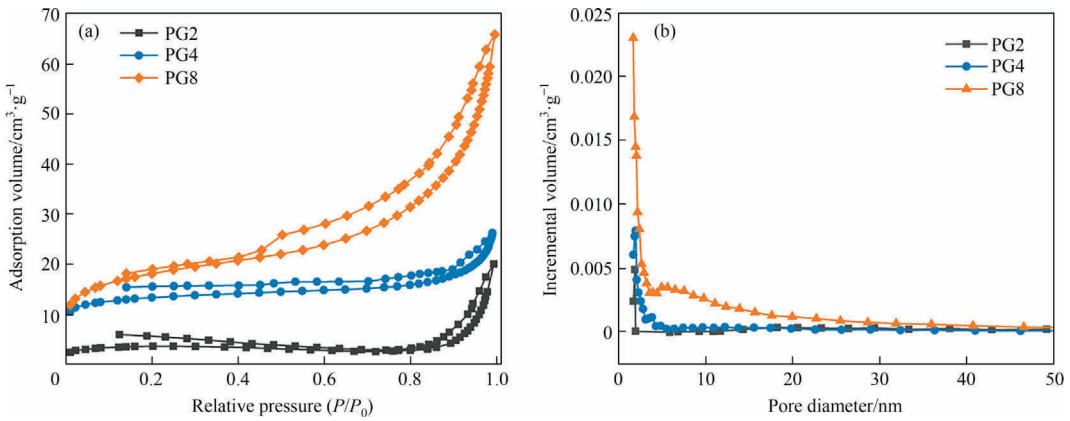

Fig. 4. (a) N_2 adsorption–desorption isotherms and (b) pore size distribution of PG2, PG4 and PG8.

$$\frac{\partial C}{\partial t} = D_{\text{eff}}\left(\frac{\partial^2 C}{\partial x^2}\right) \tag{3}$$

The diffusion properties can be quantified using the following relation as the internal diffusion is considered rate controlled [40]:

$$\frac{q_t}{q_e} = \frac{2}{\sqrt{\pi}}\sqrt{\frac{D_{\text{eff}}}{L^2}\times t} = \frac{2}{\sqrt{\pi}}\sqrt{\frac{t}{\tau}} \tag{4}$$

where D_{eff} is the diffusivity, L is the diffusion length, and t is time. τ^{-1} is the characteristic diffusion time constant, which could be calculated from Eq. (4).

Fig. 5(b) depicts the linear relationship between the absorption fraction of phenol and the square root of the diffusion time. Interestingly, at the initial diffusion stage, the characteristic diffusion time constant of phenol over PG4 and PG8 were lower than PG2. Presumably, this is because almost all active sites are within the multichannel framework rather than on the surface. Phenol cannot immediately interact with active sites within the multichannel framework. Instead, the phenol was first adsorbed on the outer surface of PG2 and then transported to the solution environment without passing through GO channels.

However, the adsorption efficiency decreases with further increase of the GO layer. As designated in Fig. 5(c), the phenol adsorption capability over PG12 and PG20 was lower than that of

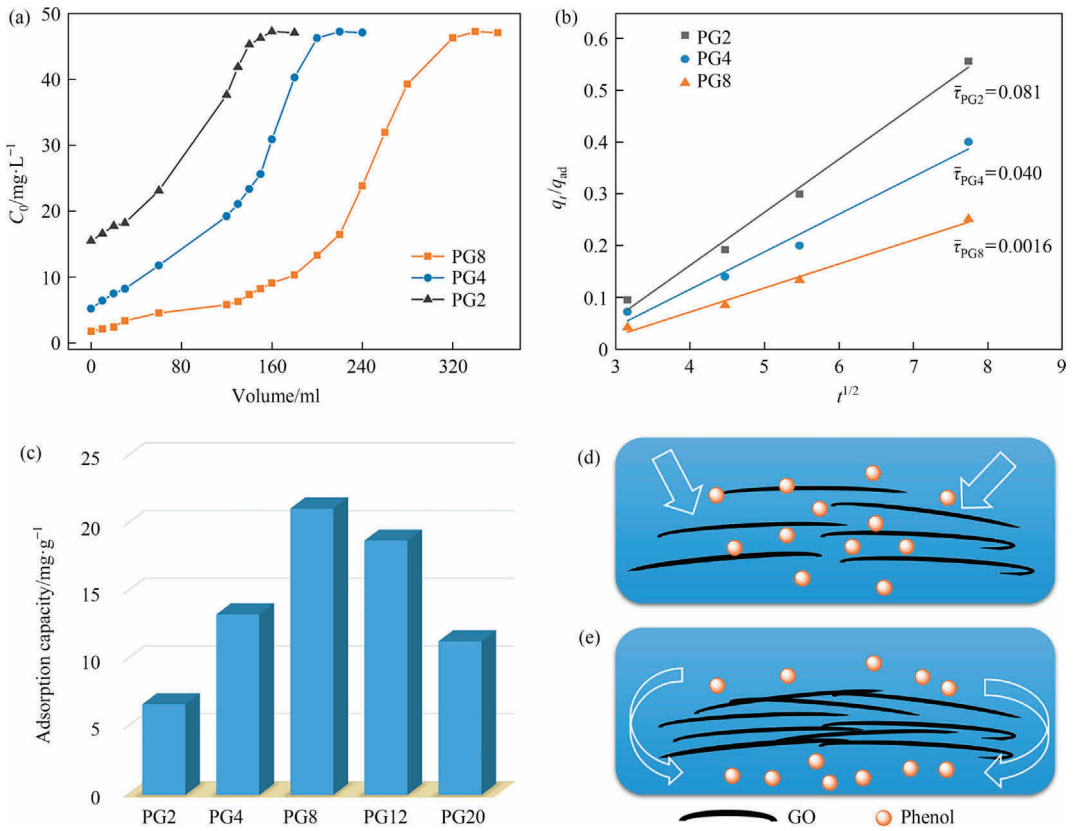

Fig. 5. (a) Penetration curves of filtration experiments of phenol on PG2, PG4 and PG8; (b) phenol uptake curves of PG2, PG4 and PG8; (c) phenol adsorption amount of the PG2, PG4, PG8, PG12 and PG20; schematic illustration for phenol molecular transport of (d) PG8 and (e) PG20.

PG8. When more GO were introduced on the support, it may block the permeating channels (as illustrated in Fig 5(e)), resulting in increased diffusion resistance in the mass transfer reaction [25]. As can be seen in Fig. S6, the channel volume is squeezed by the stacked GO sheets, which may cover some accessible active sites and thus reduce the adsorption performance.

3.3. Adsorption kinetics analysis

For further confirmation of diffusion behavior, the experimental data were fitted *via* the intraparticle diffusion model as follow [41]:

$$q_t = K_i \times t^{\frac{1}{2}} + C \tag{5}$$

where K_i (mg·g^{-1}·min$^{1/2}$), C (mg·g^{-1}) are the rate constant and intraparticle diffusion constant, respectively.

As shown in Fig. 6(a), the adsorption kinetics of PG2, PG4 and PG8 were found to have similar trends. Obviously, three linear regions were presented in each plot, suggesting that more than one stage influences the adsorption process. The first process can be described as film diffusion of solute molecules, *i.e.,* diffusion of contaminant molecules through the solution environment to the outer surface of the GO (Fig. 6(b)). In this phase, the adsorbed molecules preferentially transfer to the boundary layer according to the Fick's law. The second process is the intralayer diffusion process, which describes a progressive adsorption phase. In this stage, molecules are transferred from the external surface to the internal channels of the GO film, with intraparticle diffusion being dominant. Finally, the adsorption process achieved dynamic equilibrium.

The various parameters of interparticle diffusion model are exhibited in Table 1. The K_i values of all adsorbents obeyed the order PG8 > PG4 > PG2, with the best diffusion performance of the elucidated phenol molecules being PG8. The values of intercept C obtained from the plots q_t *versus* $t^{1/2}$ reflect the boundary layer thickness [41]. The result was found to be in contrary to those of dynamic adsorption, which might attribute to the different diffusion process. For better assess the adsorption performance, the pseudo-first-order kinetic model and pseudo-second-order kinetic model were further analyzed (see the corresponding parameters and related fitting of kinetic models in Supplementary Material, Table S1 and Fig. S7).

As a comparative experiment, the removal of phenol by GO is shown in Fig. S8. Although the adsorption capacity of PG8 is lower than that of GO, it still achieves 62% of the adsorption performance of GO. Also, the PG8 membrane exhibited comparable phenol removal efficiency under similar conditions compared to other reports (Table S2). In addition, Fig. S9 shows the regeneration of PG8 membrane after five cycles. Each regeneration was performed with hot water and the phenol saturation of the adsorbent was reduced from 22 mg·g^{-1} to 17 mg·g^{-1}, as expected.

3.4. Adsorption mechanism of GO multichannel architecture

The adsorption performance is mainly controlled by two dominant factors, *i.e.* multistage channels and active sites. Pollutant molecules could be captured in three water pathway: across defect pores of GO, through inter-edge areas [42] and inside channels [43,44] (Fig. 7(a)). By comparison with the other two conditions, the last one is more likely to allow the flow of contaminant molecules within the channel and, therefore, contributes the most to the removal of contaminants. Although the GO channel was obtained from free deposition and cannot be precisely controlled, it still roughly reflects the general differences of each sample. The multichannel structure is sufficient to bring the contaminants into contact, extending the overall diffusion pathway and facilitat-

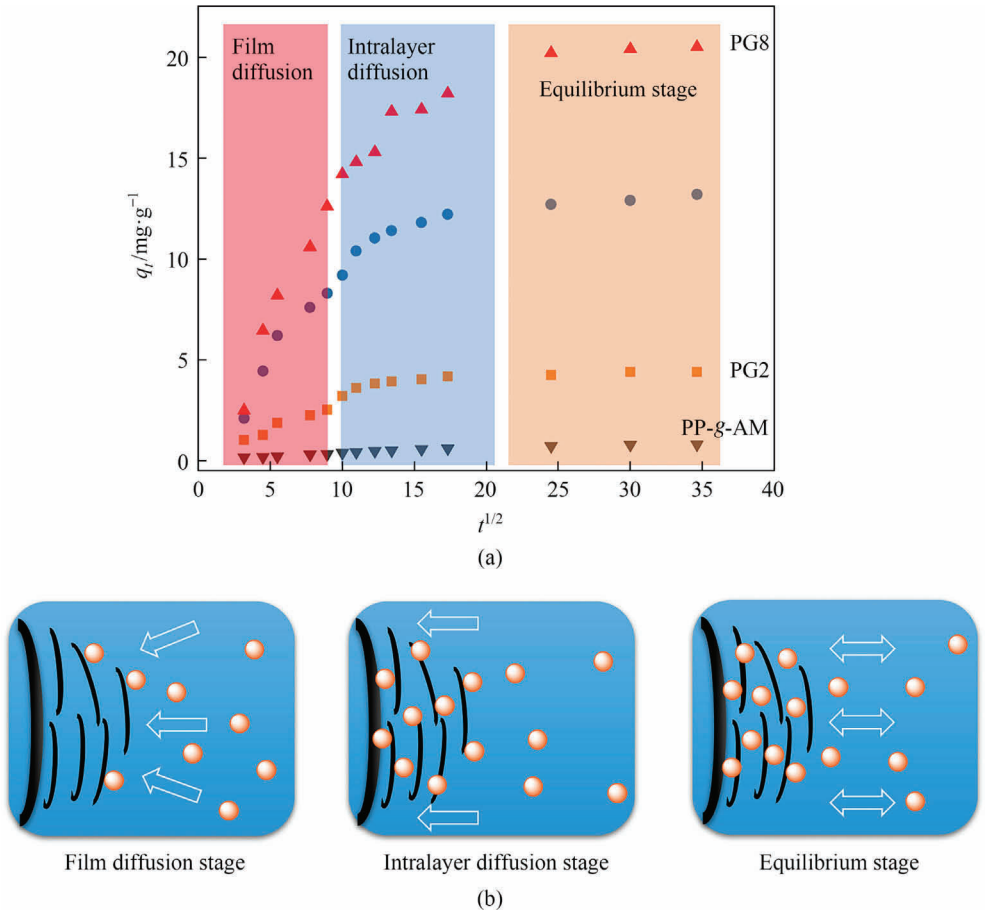

Fig. 6. The adsorption kinetics of (a) phenol on PP-g-AM substrate, PG2, PG4 and PG8 and (b) schematics of diffusion process.

Table 1
Kinetic model parameters of adsorption for phenol

Adsorbents	Target contaminant	Intraparticle diffusion model			h/mg·g^{-1}·min^{-1}	$t^{1/2}$/min	q_e/mg·g^{-1}
		K_i/min^{-1}	C	R^2			
PP-*g*-AM	Phenol	0.03	0.03	0.986	0.005	127.71	0.77
PG2		0.24	1.91	0.913	0.10	42.19	4.56
PG4		0.68	1.76	0.916	0.30	45.62	13.84
PG8		1.06	0.45	0.928	0.36	57.73	21.22

ing the internal transfer of contaminants from the solution to the active site.

Moreover, the adsorption capacity depends strongly on the active sites, as confirmed by FT-IR and XPS results. These active sites, such as oxygen-containing groups and amino functional groups, are potential adsorption sites for various contaminants [45,46]. Besides, as one of the essential introductory adsorption forces, π-π interaction may lead to the preferred adsorption sites (Fig. 7(b)) [47]. In other words, these active sites could increase the adsorption affinity of phenol.

3.5. DFT calculations

In order to further explain the adsorption sites, smaller GO-PEI model was employed. The optimized stable structures of GO-PEI channel and phenol are shown in Fig. S10. The total density of states (DOS) of GO and GO-PEI were performed to explain the interactions between GO and PEI. As indicated in Fig. S11, the bandgap of GO is zero near Fermi level. After decorating the PEI on GO, a change in the Fermi level was found. A bandgap is obtained closer to the Fermi level, which means stronger interaction between the GO and PEI. The projected density of states (PDOS) spectrum is presented in Fig. 8(a) and (b), which represent two cases of GO-PEI and GO-PEI-Phenol. The 2p orbitals of O atom and 1s orbitals of H atom are holding a dominant position near the Fermi level as phenol molecule is adsorbed on GO-PEI. It is obvious that 2p orbitals of O and 1s orbitals of H overlap near the Fermi level, which means that the existing interaction between O and H became stronger (Fig. 8(c)). On the contrary, no overlap occurred for orbitals of N and H near the Fermi level in the phenol adsorption process (Fig. 8(d)). We can conclude that the orbital coupling between O and H makes the electronic structure change after phenol molecule adsorption. Thus, the adsorption of phenol is assigned to the hydrogen bond dominated by oxygen-containing groups.

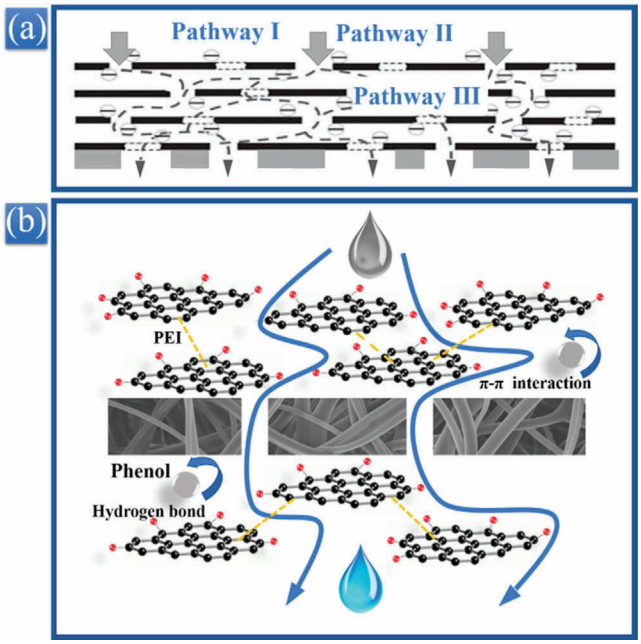

Fig. 7. (a) Schematic illustration diffusion process within GO multichannel; (b) adsorption mechanism of phenol by PG*n*.

In addition, to explore the favorable adsorption sites, the interaction energy E_I was calculated as follows:

$$E_I = E_{GO-PEI-phenol} - E_{GO-PEI} - E_{phenol} \quad (6)$$

where $E_{GO\text{-}PEI}$, E_{phenol}, and $E_{GO\text{-}PEI\text{-}phenol}$ are corresponding to the total energies of the coagulation GO-PEI, phenol, and the combined GO-PEI-phenol system, respectively. To investigate the favorable adsorption sites, the interaction energies of three possible adsorption sites for phenol were calculated. The adsorption energies of the three possible adsorption sites were found to be different, with calculated results of −1.77 eV, −1.52 eV and −2.47 eV, respectively. As presented in Fig. 9, in contrast to amino functional groups, phenol molecules always tend to adsorb to oxygen-containing functional groups, even if the phenol molecule is placed near the amino functional group. Liu *et al.* [46] reported that the oxygen-containing group can form hydrogen bonds with phenol, which is considered the preferred adsorption site. By combining the results of PDOS, we can conclude that hydrogen bond formed by oxygen-containing groups is more preferential than amino functional groups. As registered in Fig. 9(c), the vertical distance between GO and phenol is about 0.38 nm, compatible with the reported π-π interaction distance [48]. Based on the E_I calculated by DFT, the preferential adsorption configuration was prefer determined by the face-to-face π-π interaction toward phenol lying down on the GO.

The oxygen-containing groups present on GO play a crucial role in the adsorption process. In order to determine which functional group is more dominant in the adsorption of phenol, the strength of the interaction between phenol and carboxyl, epoxy and hydroxyl groups was investigated. As a result, carboxyl (−1.17 eV) was found to interact more strongly with phenol than epoxy (−0.98 eV) and hydroxyl groups (−0.79 eV). Considering that the favorable adsorption sites mainly determined by π-π interaction, the most favorable adsorption region might be the interface consist of π-π interaction and carboxyl.

3.6. Adsorption efficiency of other contaminants

The adsorption efficiency of PG*n* toward MO and Cr(VI) was also explored. As seen in Fig. 10, PG8 excelled in the dynamic adsorption of MO and Cr(VI) with 148.9 $mg \cdot g^{-1}$ and 50.4 $mg \cdot g^{-1}$, respectively. Since most oxygen-containing groups of GO were occupied by the amino groups of PEI chains, the adsorption of MO and Cr (VI) were primarily due to the electrostatic attractions between the negative charges of MO/Cr(VI) and the positive charges of the amino groups on the PEI chains (Fig. S12) [32,49]. Besides the electrostatic interaction, a strong acting force with Cr(VI) could also come from complexation and coordination of the carboxyl groups of the GO and the amino groups of the PEI [50,51]. Furthermore, π-π interaction and hydrogen bonding also favor the adsorption of MO [52,53]. The adsorption kinetics of these pollutants are described in detail, as revealed in Fig. S13 and Table S3&S4.

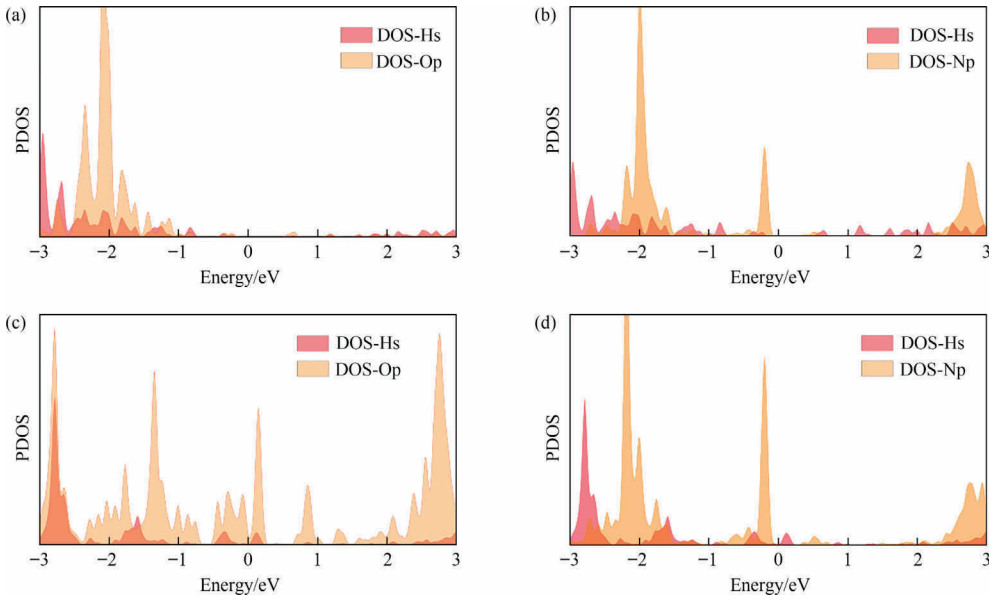

Fig. 8. PDOS of different systems. 2p orbitals of O and 1s orbitals of H in GO-PEI (a) and GO-PEI-Phenol (c) systems; 2p orbitals of N and 1s orbitals of H in GO-PEI (b) and GO-PEI-Phenol (d) systems.

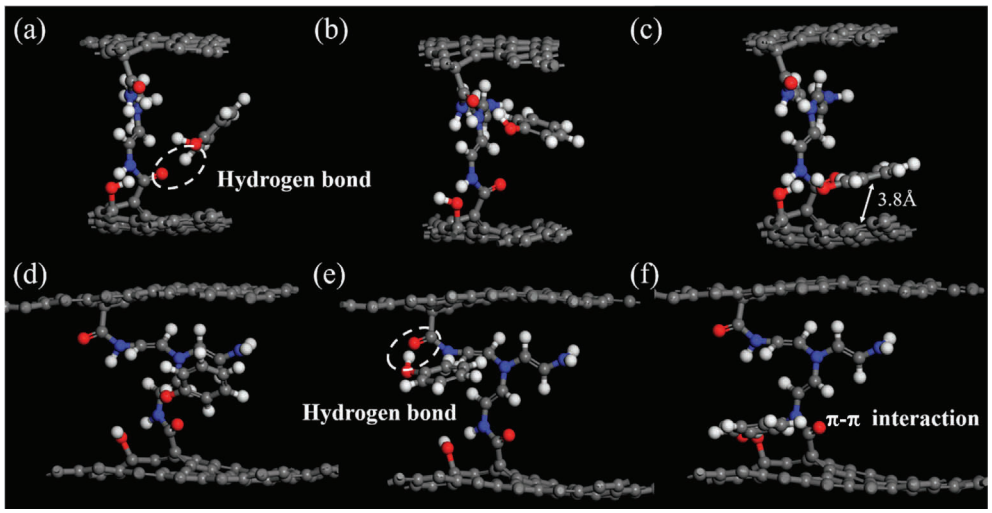

Fig. 9. Phenol adsorption conformations in the GO channel. (a), (d); (b), (e) and (c), (f) represent the final three stable conformation of phenol when it was initially placed at different positions (1 Å=0.1 nm).

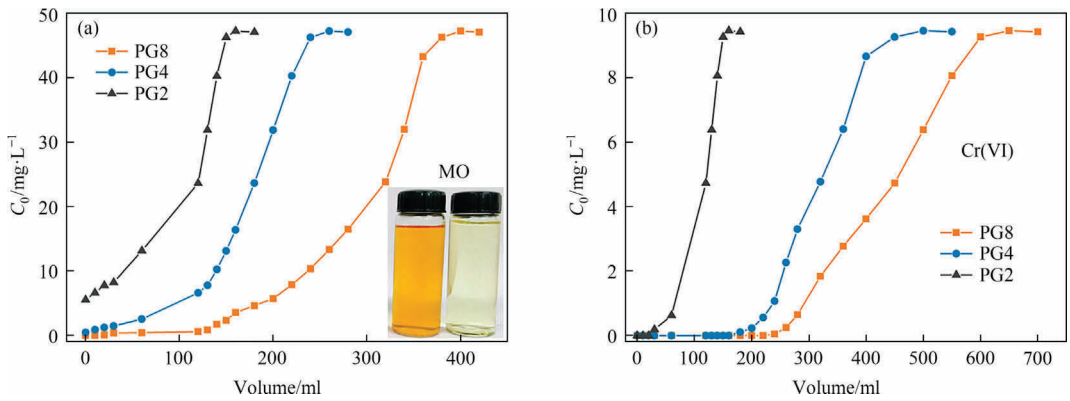

Fig. 10. Penetration curves of filtration experiments of (a) MO and (b) Cr(VI) on PG2, PG4 and PG8.

4. Conclusions

A facile LbL approach for the construction of GO membrane with multichannel has been demonstrated in this work, which was alternating stacked by GO and multibranched PEI. Phenol was used as molecular probe to determine the relevant adsorption behavior within the GO multichannel. Characterizations results clearly show that the PG*n* has a multichannel structure with abundant accessible active sites that favored to the diffusion and binding of phenol from water. The high adsorption capacity of PG8 is due to its multi-channel structure, which prolongs the unconstrained dispersion pathway of phenol and ensures the openness of the adsorption site to phenol molecules. DFT calculation results explicate that hydrogen bonds created by oxygen-containing groups may be a possible adsorption site for phenol than amino functional groups. The interfaces that consist of strong π-π interaction and hydrogen bonds formed by carboxyl may be the preferred region interacting with phenol. Given the recent upsurge in membrane technology development, this study provides fundamental insights into clean water technology for multilevel membrane channels.

Declaration of Competing Interest

The authors declare that they have no known competing financial interests or personal relationships that could have appeared to influence the work reported in this paper.

Acknowledgements

This research was supported by the National Natural Science Foundation of China (22078269 and 51708406).

Supplementary Material

Supplementary data to this article can be found online at https://doi.org/10.1016/j.cjche.2021.12.029, including fabrication of PP-*g*-AM; pore diameter distribution; SEM image, FTIR spectra, UV absorption spectra, N_2 adsorption–desorption isotherms and pore size distribution of GO; XPS spectra; water contact angle; SEM cross sections of PG4 and PG20; adsorption kinetics of phenol; adsorption kinetics of phenol on GO; regeneration of PG8 membrane after five cycles; optimized stable structure of graphene oxide, phenol and GO-PEI channel; Density of states (DOS) of the different systems of GO and GO-PEI; adsorption kinetics of MO and Cr(VI); Zeta potential curves.

References

[1] G.P. Liu, W.Q. Jin, N.P. Xu, Graphene-based membranes, *Chem. Soc. Rev.* 44 (15) (2015) 5016–5030.
[2] B. Mi, Materials science. Graphene oxide membranes for ionic and molecular sieving, *Science* 343 (6172) (2014) 740–742.
[3] R.R. Nair, H.A. Wu, P.N. Jayaram, I.V. Grigorieva, A.K. Geim, Unimpeded permeation of water through helium-leak-tight graphene-based membranes, *Science* 335 (6067) (2012) 442–444.

[4] Y. Liu, Y. Huang, X.F. Duan, Van der Waals integration before and beyond two-dimensional materials, *Nature* 567 (7748) (2019) 323–333.
[5] F. Perreault, A. Fonseca de Faria, M. Elimelech, Environmental applications of graphene-based nanomaterials, *Chem. Soc. Rev.* 44 (16) (2015) 5861–5896.
[6] G. Ersan, O.G. Apul, F. Perreault, T. Karanfil, Adsorption of organic contaminants by graphene nanosheets: A review, *Water Res.* 126 (2017) 385–398.
[7] O.G. Apul, Q.L. Wang, Y. Zhou, T. Karanfil, Adsorption of aromatic organic contaminants by graphene nanosheets: Comparison with carbon nanotubes and activated carbon, *Water Res.* 47 (4) (2013) 1648–1654.
[8] J. Wang, B.L. Chen, B.S. Xing, Wrinkles and folds of activated graphene nanosheets as fast and efficient adsorptive sites for hydrophobic organic contaminants, *Environ. Sci. Technol.* 50 (7) (2016) 3798–3808.
[9] H. Jabeen, V. Chandra, S. Jung, J.W. Lee, K.S. Kim, S.B. Kim, Enhanced Cr(vi) removal using iron nanoparticle decorated graphene, *Nanoscale* 3 (9) (2011) 3583.
[10] M.H. Xu, J. Chai, N.T. Hu, D. Huang, Y.X. Wang, X.L. Huang, H. Wei, Z. Yang, Y.F. Zhang, Facile synthesis of soluble functional graphene by reduction of graphene oxide *via* acetylacetone and its adsorption of heavy metal ions, *Nanotechnology* 25 (39) (2014) 395602.
[11] G.X. Zhao, J.X. Li, X.M. Ren, C.L. Chen, X.K. Wang, Few-layered graphene oxide nanosheets as superior sorbents for heavy metal ion pollution management, *Environ. Sci. Technol.* 45 (24) (2011) 10454–10462.
[12] P. Yu, H.-Q. Wang, R.-Y. Bao, Z. Liu, W. Yang, B.-H. Xie, M.-B. Yang, Self-assembled sponge-like chitosan/reduced graphene oxide/montmorillonite composite hydrogels without cross-linking of chitosan for effective Cr(VI) sorption, *ACS Sustain. Chem. Eng.* 5 (2017) 1557–1566.
[13] Y. Shen, X.Y. Zhu, B.L. Chen, Size effects of graphene oxide nanosheets on the construction of three-dimensional graphene-based macrostructures as adsorbents, *J. Mater. Chem. A* 4 (31) (2016) 12106–12118.
[14] J. Zhao, Z.Y. Wang, J.C. White, B.S. Xing, Graphene in the aquatic environment: Adsorption, dispersion, toxicity and transformation, *Environ. Sci. Technol.* 48 (17) (2014) 9995–10009.
[15] L. Chen, G.S. Shi, J. Shen, B.Q. Peng, B.W. Zhang, Y.Z. Wang, F.G. Bian, J.J. Wang, D.Y. Li, Z. Qian, G. Xu, G.P. Liu, J.R. Zeng, L.J. Zhang, Y.Z. Yang, G.Q. Zhou, M.H. Wu, W.Q. Jin, J.Y. Li, H.P. Fang, Ion sieving in graphene oxide membranes *via* cationic control of interlayer spacing, *Nature* 550 (7676) (2017) 380–383.
[16] J.J. Deng, Y. You, H. Bustamante, V. Sahajwalla, R.K. Joshi, Mechanism of water transport in graphene oxide laminates, *Chem. Sci.* 8 (3) (2017) 1701–1704.
[17] D. Cohen-Tanugi, J.C. Grossman, Water desalination across nanoporous graphene, *Nano Lett.* 12 (7) (2012) 3602–3608.
[18] T. Lee, B.S. Kim, Two-dimensional designer nanochannels for controllable ion transport in graphene oxide nanomembranes with tunable sheet dimensions, *ACS Appl. Mater. Interfaces* 12 (11) (2020) 13116–13126.
[19] R. Zambare, X.X. Song, S. Bhuvana, J.S. Antony Prince, P. Nemade, Ultrafast dye removal using ionic liquid–graphene oxide sponge, *ACS Sustainable Chem. Eng.* 5 (7) (2017) 6026–6035.
[20] H.B. Huang, Y.L. Ying, X.S. Peng, Graphene oxide nanosheet: An emerging star material for novel separation membranes, *J. Mater. Chem. A* 2 (34) (2014) 13772–13782.
[21] T. Ghosh, C. Biswas, J. Oh, G. Arabale, T. Hwang, N.D. Luong, M.H. Jin, Y.H. Lee, J. D. Nam, Solution-processed graphite membrane from reassembled graphene oxide, *Chem. Mater.* 24 (3) (2012) 594–599.
[22] Z.K. Zheng, R. Grünker, X.L. Feng, Synthetic two-dimensional materials: A new paradigm of membranes for ultimate separation, *Adv. Mater.* 28 (31) (2016) 6529–6545.
[23] P.C. Bandara, E.T. Nadres, D.F. Rodrigues, Use of response surface methodology to develop and optimize the composition of a chitosan–polyethyleneimine–graphene oxide nanocomposite membrane coating to more effectively remove Cr(VI) and Cu(II) from water, *ACS Appl. Mater. Interfaces* 11 (19) (2019) 17784–17795.
[24] X.F. Ou, X.H. Yang, J.Q. Zheng, M.X. Liu, Free-standing graphene oxide–chitin nanocrystal composite membrane for dye adsorption and oil/water separation, *ACS Sustainable Chem. Eng.* 7 (15) (2019) 13379–13390.
[25] M. Musielak, A. Gagor, B. Zawisza, E. Talik, R. Sitko, Graphene oxide/carbon nanotube membranes for highly efficient removal of metal ions from water, *ACS Appl. Mater. Interfaces* 11 (31) (2019) 28582–28590.
[26] S.J. Yu, H.W. Pang, S.Y. Huang, H. Tang, S.Q. Wang, M.Q. Qiu, Z.S. Chen, H. Yang, G. Song, D. Fu, B.W. Hu, X.X. Wang, Recent advances in metal-organic framework membranes for water treatment: A review, *Sci. Total. Environ.* 800 (2021) 149662.
[27] Q. Li, Z.S. Chen, H.H. Wang, H. Yang, T. Wen, S.Q. Wang, B.W. Hu, X.K. Wang, Removal of organic compounds by nanoscale zero-valent iron and its composites, *Sci. Total. Environ.* 792 (2021) 148546.
[28] L.P. Liang, F.F. Xi, W.S. Tan, X. Meng, B.W. Hu, X.K. Wang, Review of organic and inorganic pollutants removal by biochar and biochar-based composites, *Biochar* 3 (3) (2021) 255–281.
[29] X.Y. Zhou, F.F. Wang, Y.L. Ji, W.T. Chen, J.F. Wei, Fabrication of hydrophilic and hydrophobic sites on polypropylene nonwoven for oil spill cleanup: Two dilemmas affecting oil sorption, *Environ. Sci. Technol.* 50 (7) (2016) 3860–3865.
[30] J. Tian, J.F. Wei, H. Zhang, Z.Y. Kong, Y.W. Zhu, Z. Qin, Graphene oxide-functionalized dual-scale channels architecture for high-throughput removal of organic pollutants from water, *Chem. Eng. J.* 359 (2019) 852–862.
[31] D. Chen, X.Y. Wang, T.X. Liu, X.D. Wang, J. Li, Electrically conductive poly(vinyl alcohol) hybrid films containing graphene and layered double hydroxide fabricated *via* layer-by-layer self-assembly, *ACS Appl. Mater. Interfaces* 2 (7) (2010) 2005–2011.
[32] Q. Zhao, X.Y. Zhu, B.L. Chen, Stable graphene oxide/poly(ethyleneimine) 3D aerogel with tunable surface charge for high performance selective removal of ionic dyes from water, *Chem. Eng. J.* 334 (2018) 1119–1127.
[33] Q. Liu, J.B. Shi, J.T. Sun, T. Wang, L.X. Zeng, G.B. Jiang, Graphene and graphene oxide sheets supported on silica as versatile and high-performance adsorbents for solid-phase extraction, *Angew. Chem. Int. Ed Engl.* 50 (26) (2011) 5913–5917.
[34] W.S. Hung, C.H. Tsou, M. de Guzman, Q.F. An, Y.L. Liu, Y.M. Zhang, C.C. Hu, K.R. Lee, J.Y. Lai, Cross-linking with diamine monomers to prepare composite graphene oxide-framework membranes with varying d-spacing, *Chem. Mater.* 26 (9) (2014) 2983–2990.
[35] Y.R. Yu, Y. Shu, L. Ye, *In situ* crosslinking of poly (vinyl alcohol)/graphene oxide-glutamic acid nano-composite hydrogel as microbial carrier: Intercalation structure and its wastewater treatment performance, *Chem. Eng. J.* 336 (2018) 306–314.
[36] X.L. Zhou, Y.K. Zeng, X.B. Zhu, L. Wei, T.S. Zhao, A high-performance dual-scale porous electrode for vanadium redox flow batteries, *J. Power Sources* 325 (2016) 329–336.
[37] C.J. Bae, C.K. Erdonmez, J.W. Halloran, Y.M. Chiang, Design of battery electrodes with dual-scale porosity to minimize tortuosity and maximize performance, *Adv. Mater.* 25 (9) (2013) 1254–1258.
[38] M.Y. Kim, K. Lee, M. Choi, Cooperative effects of secondary mesoporosity and acid site location in Pt/SAPO-11 on *n*-dodecane hydroisomerization selectivity, *J. Catal.* 319 (2014) 232–238.
[39] J.C. Groen, W.D. Zhu, S. Brouwer, S.J. Huynink, F. Kapteijn, J.A. Moulijn, J. Pérez-Ramírez, Direct demonstration of enhanced diffusion in mesoporous ZSM-5 zeolite obtained *via* controlled desilication, *J. Am. Chem. Soc.* 129 (2) (2007) 355–360.
[40] P. Peng, D. Stosic, A. Aitblal, A. Vimont, P. Bazin, X.M. Liu, Z.F. Yan, S. Mintova, A. Travert, Unraveling the diffusion properties of zeolite-based multicomponent catalyst by combined gravimetric analysis and IR spectroscopy (AGIR), *ACS Catal.* 10 (12) (2020) 6822–6830.
[41] X.Y. Zhou, J.F. Wei, H. Zhang, K. Liu, H. Wang, Adsorption of phthalic acid esters (PAEs) by amphiphilic polypropylene nonwoven from aqueous solution: The study of hydrophilic and hydrophobic microdomain, *J. Hazard. Mater.* 273 (2014) 61–69.
[42] A. Bagri, C. Mattevi, M. Acik, Y.J. Chabal, M. Chhowalla, V.B. Shenoy, Structural evolution during the reduction of chemically derived graphene oxide, *Nat. Chem.* 2 (7) (2010) 581–587.
[43] D.W. Boukhvalov, M.I. Katsnelson, Y.W. Son, Origin of anomalous water permeation through graphene oxide membrane, *Nano Lett.* 13 (8) (2013) 3930–3935.
[44] N. Wei, X.S. Peng, Z.P. Xu, Understanding water permeation in graphene oxide membranes, *ACS Appl. Mater. Interfaces* 6 (8) (2014) 5877–5883.
[45] X.T. Liu, H.Y. Zhang, Y.Q. Ma, X.L. Wu, L.X. Meng, Y.L. Guo, G. Yu, Y.Q. Liu, Graphene-coated silica as a highly efficient sorbent for residual organophosphorus pesticides in water, *J. Mater. Chem. A* 1 (5) (2013) 1875–1884.
[46] F.F. Liu, J. Zhao, S.G. Wang, P. Du, B.S. Xing, Effects of solution chemistry on adsorption of selected pharmaceuticals and personal care products (PPCPs) by graphenes and carbon nanotubes, *Environ. Sci. Technol.* 48 (22) (2014) 13197–13206.
[47] H. Tang, Y. Zhao, S.J. Shan, X.N. Yang, D.M. Liu, F.Y. Cui, B.S. Xing, Wrinkle- and edge-adsorption of aromatic compounds on graphene oxide as revealed by atomic force microscopy, molecular dynamics simulation, and density functional theory, *Environ. Sci. Technol.* 52 (14) (2018) 7689–7697.
[48] Y.F. Li, H. Li, K. Zhang, K.M. Liew, The theoretical possibility of a graphene sheet spontaneously scrolling round an iron nanowire, *Carbon* 50 (2) (2012) 566–576.
[49] J.L. Xiao, W.Y. Lv, Z. Xie, Y.Q. Tan, Y.H. Song, Q. Zheng, Environmentally friendly reduced graphene oxide as a broad-spectrum adsorbent for anionic and cationic dyes *via* π–π interactions, *J. Mater. Chem. A* 4 (31) (2016) 12126–12135.
[50] F.L. Liu, S. Hua, C. Wang, M.Q. Qiu, L.M. Jin, B.W. Hu, Adsorption and reduction of Cr(VI) from aqueous solution using cost-effective caffeic acid functionalized corn starch, *Chemosphere* 279 (2021) 130539.
[51] Y.L. Zhu, X.Y. He, J.L. Xu, Z. Fu, S.Y. Wu, J. Ni, B.W. Hu, Insight into efficient removal of Cr(VI) by magnetite immobilized with *Lysinibacillus* sp. JLT12: Mechanism and performance, *Chemosphere* 262 (2021) 127901.
[52] L. Shen, Z.H. Jin, W.H. Xu, X. Jiang, Y.X. Shen, Y.P. Wang, Y.H. Lu, Enhanced treatment of anionic and cationic dyes in wastewater through live bacteria encapsulation using graphene hydrogel, *Ind. Eng. Chem. Res.* 58 (19) (2019) 7817–7824.
[53] R.M. Yu, Y.Z. Shi, D.Z. Yang, Y.X. Liu, J. Qu, Z.Z. Yu, Graphene oxide/chitosan aerogel microspheres with honeycomb-cobweb and radially oriented microchannel structures for broad-spectrum and rapid adsorption of water contaminants, *ACS Appl. Mater. Interfaces* 9 (26) (2017) 21809–21819.